Multiphysics Modeling for Combustion Instability in Paraffin-Fueled Hybrid Rocket Engines

Multi-Physics Modelling for Combustion Instability in Paraffin-Fueled Hybrid Rocket Engines

Lorenzo Casalino*, Andrea Ferrero†, Lorenzo Folcarelli ‡, Filippo Masseni§, Luca Muscará¶, and Dario Pastrone‖
Politecnico di Torino, Turin, 10129, Italy

Maria Luisa Frezzotti ** and Attilio Cretella ††
Avio S.p.A., Colleferro, 00034, Italy

Rocco Carmine Pellegrini ‡‡ and Enrico Cavallini §§
Agenzia Spaziale Italiana, Rome, 00133, Italy

The use of paraffin-based fuels is a promising approach to low regression rate in hybrid rocket engines and the capability to describe and predict combustion instability in the presence of liquefying fuels becomes an enabling step towards the application of hybrid rockets in a wide range of space transportation systems. In this work, a multi-physics model having this purpose is presented and discussed. The model is based on a network of submodels, in which the chamber gas dynamics is described by a quasi-1D Euler model for reacting flows while thermal diffusion in the grain is described by the 1D heat equation in the radial direction. An artificial neural network is introduced to reduce the computational cost required by the chemical submodel. A sensitivity analysis is performed to identify the key parameters which have the largest influence on combustion instability and to evaluate the predictive capability of the model despite uncertainty introduced with the necessary modelling simplifications. Results are presented considering two test cases with different oxidizers: hydrogen peroxide and gaseous oxygen. The procedure shows good agreement with experimental results available in the literature.

Nomenclature

A = cross section area

*Full professor, Department of Mechanical and Aerospace Engineering, Corso Duca degli Abruzzi 24, 10129 Turin, Italy, AIAA Member
†Assistant Professor, Department of Mechanical and Aerospace Engineering, Corso Duca degli Abruzzi 24, 10129 Turin, Italy, AIAA Member
‡PhD student, Department of Mechanical and Aerospace Engineering, Corso Duca degli Abruzzi 24, 10129 Turin, Italy
§Assistant Professor, Department of Mechanical and Aerospace Engineering, Corso Duca degli Abruzzi 24, 10129 Turin, Italy
¶PhD student, Department of Mechanical and Aerospace Engineering, Corso Duca degli Abruzzi 24, 10129 Turin, Italy
‖Full Professor, Department of Mechanical and Aerospace Engineering, Corso Duca degli Abruzzi 24, 10129 Turin, Italy, AIAA Associate Fellow
**PhD Designer, Solid Propulsion Design Department, Via Degli Esplosivi 1, 0034 Colleferro, Italy
††Program Manager, Research Program Managment, Via Degli Esplosivi 1, 0034 Colleferro, Italy
‡‡Space Transportation and In-Orbit Servicing Dept., Via del Politecnico snc, 00133 Rome, Italy
§§Head of Space Transportation and In-Orbit Servicing Dept., Via del Politecnico snc, 00133 Rome, Italy, AIAA Senior Member

A_h	=	Arrhenius equation pre-exponential factor
A_p	=	port area
a	=	regression rate correlation coefficient
B	=	aerodynamic blowing parameter
B_t	=	thermochemical blowing parameter
C_f	=	skin friction coefficient
c_p	=	specific heat
d	=	derivative
E	=	total energy per unit mass
E_a	=	activation energy
e	=	internal energy per unit mass
$\boldsymbol{F}$	=	conservative fluid dynamics fluxes vector
G	=	mass flux
h	=	enthalpy, thickness of liquid layer
h_v	=	effective enthalpy of vaporization
K	=	swirl correction factor
k_b	=	exponent of the skin friction coefficient ratio
L_m	=	latent heat of fusion
L_v	=	latent heat of vaporization
l_p	=	section perimeter
m	=	mass
N	=	number of chemical species
N_G	=	number of gaseous species
N_S	=	number of species
o/f	=	mixture ratio
p	=	pressure
q	=	pre-exponential factor of the skin friction coefficient ratio
$\boldsymbol{Q}$	=	conservative fluid dynamics variables vector
$\dot{Q}$	=	heat flux
R	=	specific gas constant
R_u	=	universal gas constant
Re_x	=	local Reynolds number

$\dot{r}$	=	total regression rate
$\dot{r}_l$	=	relative liquid velocity
$\dot{r}_m$	=	regression rate of the liquid-solid interface
$\dot{r}_v$	=	evaporation regression rate
S_n	=	Swirl Number
St	=	Strouhal Number
T	=	temperature
t	=	time
u	=	axial speed
v	=	radial speed
w	=	molecular weight
x	=	axial location
Y	=	mass fraction
y	=	radial location
α	=	thermal diffusivity
α_e	=	exponential coefficient
α_g	=	gas phase absorptivity
β_e	=	exponential coefficient
γ	=	specific heat ratio
γ_s	=	isentropic exponent
Δh	=	flame-surface enthalpy difference
Δh^0	=	enthalpy of formation
Δt	=	time step
δ	=	solid phase thermal thickness
∂	=	partial derivative
ϵ	=	mixture fraction
ϵ_g	=	gas phase emissivity
ϵ_w	=	liquid surface emissivity
λ	=	thermal conductivity
μ	=	dynamic viscosity
ρ	=	density
σ	=	Stefan-Boltzmann constant

τ	=	delay time
ω	=	production rate from pyrolysis

Superscripts

$\dot{}$	=	time derivative
n	=	n-th time step

Subscripts

0	=	reference condition
a	=	ambient
b	=	gas flame location
bl	=	boundary layer
c	=	chamber, convective
e	=	external flow
ent	=	entrainment
F	=	fuel
g	=	grid
i	=	i-th term
int	=	interface
l	=	liquid
loc	=	local
m	=	melting
new	=	new
old	=	old
r	=	radiative
ref	=	reference value
s	=	solid
v	=	vaporization
w	=	wall

Chemical Formula

C_2H_4	=	Ethylene
$C_{32}H_{66}$	=	paraffin wax
CO	=	carbon monoxide
CO_2	=	carbon dioxide

H	=	atomic hydrogen
H_2	=	hydrogen
H_2O	=	water
H_2O_2	=	hydrogen peroxide
O	=	atomic oxygen
O_2	=	oxygen
OH	=	hydroxide

I. Introduction

HYBRID rocket engines (HREs) represent a promising alternative to both solid rocket motors and liquid rocket engines. They have throttling and restart capabilities with performance similar to storable liquids while being safer and having lower costs. Moreover, they may employ greener propellants, reducing pollution and handling risks, and their "pure fuel" grains present less manufacturing and operation hazards than solid rocket motors grains which contain both fuel and oxidizer.

However, there are some drawbacks which prevent the widespread use of HREs. First of all, the regression rate obtained with classical fuels (high-density polyethylene, hydroxyl-terminated polybutadiene, ...) is small and this poses severe limitations [1]. In order to mitigate this problem, the use of liquefying fuels has been proposed and several research studies have been carried out on the behaviour of these propellants [2–4]. The key phenomenon which makes liquefying fuels interesting is the so-called entrainment: a layer of liquid or supercritical fuel develops on the grain surface and droplets are separated and injected into the gas because of hydrodynamic instability. The study of liquefying fuels based on paraffin has been carried out both experimentally [3, 5–8] and numerically [9–12] and represents an active research area.

A second drawback related to HREs is represented by several mechanisms which can lead to combustion instability [13]. For these reasons, the capability to modelling combustion instabilities in HREs based on liquefying fuels represents an important goal for the further development of this technology.

More specifically, hybrid rockets have been shown to be characterized by low-frequency instabilities [14], as a wide literature of tests performed on HREs reports [3, 15–18]. Karabeyoglu addresses the low-frequency instabilities in HREs as the product of the coupling of three phenomena: the blocking of heat transfer by radial injection of fuel mass, the thermal transients in the solid grain and the boundary-layer dynamics [14]. However, due to its importance in any operational scenario, full understanding of combustion chamber instability in HREs is still an active field of research [19–22]. In particular, a lot of effort has been made to correctly modelize the internal ballistics of paraffin-based hybrid rockets [23–25], also with a focus on the effects of the radiative heat flux [26] and the swirl injection of the oxidizer [27].

Moreover, the capability of a 1D model to predict the onset of instability in the combustion chamber is exhibited by Karthikeyan and Shimada in Ref. [28] and by Karabeyoglu in Ref. [14]. Hence, to capture this complex phenomenon, here a 1D multi-physics model for HREs is outlined and discussed, extending the previous works presented in Ref. [29], with the inclusion of the physics of liquefying fuels, and in Ref. [30], with the addition of a chemical model for gaseous oxygen.

The model is based on a network of submodels. The chamber gasdynamics is described by a quasi-1D Euler model, utilizing the same approach outlined by Karthikeyan and Shimada in Ref. [28]. The chamber gasdynamics is then coupled with the thermal model, with thermal diffusion in the grain being described by a 1D heat equation in the radial direction, following the work of Barato et al. [31], and the convective heat flux being approximated using the relations found by Karebeyoglu in Ref. [32]. The chemical composition inside the chamber is obtained by assuming that the shifting equilibrium hypothesis holds: a surrogate model based on artificial neural networks is proposed to reduce the computational cost associated to the calculation of the equilibrium composition. Moreover, some complex phenomena like the entrainment and the boundary layer delay profile are described by the empirical models proposed by Karabeyouglu respectively in Ref. [16] and Ref. [14]. Finally, the radiative heat flux is approximated assuming the flame temperature being significantly higher than the grain surface temperature and, for hydrogen peroxide, a swirl model is presented.

The need to introduce strong modelling simplifications introduces significant uncertainty in the capability of the numerical simulation. This is particularly true for the phenomena related to combustion instability. For this reason, a sensitivity analysis is performed in order to identify the key parameters which have the largest influence on combustion instability. Results are presented on two test cases which refer to a paraffin-based grain burnt with hydrogen peroxide [33] and gaseous oxygen [16].

The article is organized as described in the following. In Section II the adopted discretization techniques are presented together with all the physical models, except for chemical models which are described in Section III. In Section IV, results for Hydrogen Peroxide are presented: after a preliminary calibration of the model based on literature data [33], results of unsteady cases with combustion instability and sensitivity analysis are shown. In the same manner, Section V contains steady and unsteady results when gaseous oxygen is used as oxidizer.

II. Multi-physics Modelling and Discretization

A. Gas-dynamic Model

The flow field in the chamber is described by the quasi-1D Euler equations augmented by a transport equation for the mixture fraction ϵ, following the approach proposed in Ref. [28].

$$\frac{\partial \mathbf{Q}A}{\partial t} + \frac{\partial \mathbf{F}A}{\partial x} = \mathbf{S}_{Q1D} + \mathbf{S}_{MASS} \tag{1}$$

$$\mathbf{Q} = (\rho, \rho u, \rho E, \rho \epsilon)^T \tag{2}$$

$$\mathbf{F} = \left(\rho u, p + \rho u^2, u(p + \rho E), \rho u \epsilon\right)^T \tag{3}$$

$$\mathbf{S}_{Q1D} = \left(0, p\frac{\partial A}{\partial x}, 0, 0\right)^T \tag{4}$$

$$\mathbf{S}_{MASS} = \left(\dot{m}_F l_p, 0, \dot{m}_F l_p \Delta h^0_{f,s}, \dot{m}_F l_p\right)^T \tag{5}$$

The variables $\dot{m}_F$ and $\Delta h^0_{f,s}$ refer to the fuel flux emitted by the grain and the related enthalpy, while ρ, p, E, u, ϵ, l_p, A_p represent density, pressure, total energy per unit mass, speed, mixture fraction, section perimeter and port area, respectively. The mixture fraction ϵ is defined according to Ref. [28]:

$$\epsilon = \frac{b_C - b_{C,2}}{b_{C,1} - b_{C,2}} \tag{6}$$

where b_C is the mole number of atomic element C per unit mass of mixture gas and 1 and 2 represent the fuel and oxidizer stream, respectively. Exploiting the chemical formulation of the oxidants used in this paper, it is possible to simplify Eq.6 as:

$$\epsilon = \frac{b_C}{b_{C,1}} \tag{7}$$

The mixture fraction is useful as a conserved quantity for the CFD simulation [28], but usually the mixture ratio o/f is an easier variable to visualize. Using the pyrolysis model explained in Section III, the relation between these two variables is expressed as follows:

$$o/f = \frac{\dot{m}_{ox}}{\dot{m}_f} = \frac{1-\epsilon}{\epsilon} \tag{8}$$

Total energy per unit mass E and the internal energy per unit mass e are evaluated for a mixture with N chemical species as:

$$E = e + \frac{u^2}{2} \tag{9}$$

$$e = \sum_{i=1}^{N} h_i Y_i - \frac{p}{\rho} \tag{10}$$

$$h_i = \Delta h_i^0 + \int_{T_0}^{T} c_{p,i} dT \tag{11}$$

where h_i, Y_i, Δh_i^0, $c_{p,i}$ represent enthalpy, mass fraction, enthalpy of formation and specific heat, respectively. The specific heat is expressed as a polynomial fitting of temperature, as NASA-9 polynomials [34]:

$$\frac{c_p}{R_u} = a_1 T^{-2} + a_2 T^{-1} + a_3 + a_4 T + a_5 T^2 + a_6 T^3 + a_7 T^4 \tag{12}$$

The source term in the energy equation can be derived imposing the energy balance at the interface between the fuel grain and the gas flow, as shown in Ref.[35]:

$$\lambda_g \frac{\partial T}{\partial y}\bigg|_{w+} + Q_{rad}^{net} - \sum_{i=1}^{Nspe} \dot{\omega}_i h_{i,w} = -G_f h_s + \lambda_s \frac{\partial T}{\partial y}\bigg|_{w-} \tag{13}$$

where y is the coordinate normal to the grain fuel, $w+$ and $w-$ are the wall locations respectively in the flow and in the solid fuel, $h_{i,w}$ represents the enthalpy of the ith product of pyrolysis, h_s the enthalpy of the solid fuel, λ_g and λ_s are conductivity respectively in the gas and in the solid fuel and Q_{rad}^{net} is the net heat flux provided by thermal radiation. Further, the fuel mass flow rate G_f and the production rate of the ith species ω_i are defined in the following way [35]:

$$G_f = (\rho v)|_w = \rho_{fuel} \cdot r \tag{14}$$

$$\omega_i = Y_i G_f - \rho D_{m,i} \frac{\partial Y_i}{\partial \eta}\bigg|_{w+} \tag{15}$$

with Y_i being the mass fraction and D_m, i the mass diffusivity of the ith species in the gas mixture. Following Ref.[35], i.e. neglecting the radiative contributions and assuming quasi-steady heat conduction in the grain, Eq.13 can be written as:

$$\lambda_g \frac{\partial T}{\partial y}\bigg|_{w+} = \sum_{i=1}^{Nspe} \omega_i h_{i,w} - G_f \Delta h_{f,s}^0 \tag{16}$$

Assuming the point of view of the gaseous flow and recalling that the species formed during pyrolysis enter the

combustion chamber giving back their enthalpies to the gaseous mixture, the source term of the energy equation in Eq.4 can be written as:

$$S_{Energy} = \dot{m}_F \, l_p \, \Delta h^0_{f,s} \tag{17}$$

Finally, the ideal gas law is assumed for all the simulated species:

$$p = \sum_{i=1}^{N} \frac{Y_i}{w_i} \rho R_u T = \rho R T \tag{18}$$

The governing equations are discretized by means of the method of lines. A second-order accurate finite volume method is chosen for space discretization. The reconstruction is limited by means of the minmod limiter and the fluxes at the interfaces are computed through the AUSM+ numerical flux [36]. Time integration is performed via a second-order accurate Runge-Kutta scheme. The simulations are performed neglecting the geometrical effects of the regression of the burning surface: the geometry of the grain is assumed to be cylindrical and the port area is assumed to be constant during the simulation.

B. Thermal Model

The source term represented by Eq. 5 in the gas dynamic equations requires to model the grain regression rate. This can be done by considering the 1D heat equation in the radial direction. In this work, a liquefying fuel represented by a paraffin wax is considered: as a result, the heat equation must be solved in the solid grain and in the liquid layer which covers the grain. Since the gas dynamic model is described by the quasi-1D Euler equations discretized along the axial direction, the equations of the thermal model are solved for each cell of the gas dynamic domain: axial conduction in the grain is neglected.

The two equations of the thermal model, written in a reference system which follows the liquid-gas interface, are defined according to Barato et al. [31]:

$$\frac{\partial T}{\partial t} = \dot{r}_l \frac{\partial T}{\partial y} + \alpha_l \frac{\partial^2 T}{\partial y^2} \tag{19}$$

$$\frac{\partial T}{\partial t} = \dot{r} \frac{\partial T}{\partial y} + \alpha_s \frac{\partial^2 T}{\partial y^2} \tag{20}$$

The grain geometry is supposed cylindrical, so cylindrical coordinates should be used. However, the radial extension of the domain considered for the heat equation is significantly smaller with respect to the grain radius and so a 1D thermal model is adopted. The relative liquid velocity $\dot{r}_l$ can be expressed as:

$$\dot{r}_l = v_l + \dot{r} = \dot{r}_m \left(\frac{\rho_s}{\rho_l} - 1 \right) + \dot{r} = \frac{\dot{m}_F}{\rho_l} \tag{21}$$

where the liquid and solid densities are taken into account through a mass balance over the liquid-solid interface. The total fuel mass flux $\dot{m}_F$ results to be the sum of two terms, the vaporization mass flux $\dot{m}_v$ and the fuel mass flux due to the entrainment mechanism $\dot{m}_{ent}$:

$$\dot{m}_F = \dot{m}_v + \dot{m}_{ent} \tag{22}$$

The vaporization mass flux is:

$$\dot{m}_v = \rho_s \dot{r}_v \tag{23}$$

The paraffin wax here considered is $C_{32}H_{66}$, which has a critical pressure of about 6.5 bar [16]. Since in typical operating conditions of a HRE the chamber pressure is larger than 6.5 bar, the fuel in the melted layer is in supercritical condition, and the surface phenomena are driven by the pyrolysis process. Therefore, the evaporation regression rate $\dot{r}_v$ is evaluated as :

$$\dot{r}_v = A_h e^{-\frac{E_a}{RT_w}} \tag{24}$$

where A_h is a constant coefficient that depends on the fuel properties. The fuel mass flux originated by the entrainment mechanism is evaluated as:

$$\dot{m}_{ent} = \rho_s \dot{r}_{ent} \tag{25}$$

The entrainment regression rate $\dot{r}_{ent}$ depends on the total regression rate through the total mass flux according to Karabeyoglu et al. [16].

$$\dot{r}_{ent} = \frac{a_{ent} G^{2\alpha_e}}{\dot{r}^{\beta_e}} \tag{26}$$

where the entrainment coefficient a_{ent} is function of the fuel properties. In agreement with Ref. [16], the values for the exponential coefficients are set to $\alpha_e = 1.5$ and $\beta_e = 2$. However, Barato et al. [37] showed that these values could lead to unrealistic regression rate curves. In the present work, the focus is on a parametric study of instability with a fixed oxidizer mass flow rate: future work will be devoted to find better approximations for the coefficients α_e and $\beta_e = 2$. In addition, the liquid-layer thickness dynamics is taken into account with the following expression:

$$\frac{dh}{dt} = \dot{r}_m - \dot{r} \tag{27}$$

As far as boundary conditions are concerned, the total heat flux at the gas-liquid (or supercritical fluid) interface has to be equal to the conductive heat transfer into the liquid (or supercritical fluid) and the heat needed for the phase transformation.

$$\dot{Q}_{tot} = \dot{m}_v L_v - \lambda_l \left.\frac{\partial T}{\partial y}\right|_{y=0} \tag{28}$$

In Eq. 28, the total heat flux is the sum of the convective and the radiative heat flux ($Q_{tot} = Q_c + Q_r$). A check is carried out in order to assess if there are actually supercritical conditions in the chamber and, in that case, L_v is set to zero, following Ref.[16] with the assumption that the pyrolysis products are in the gaseous phase due to high surface temperatures.

The boundary condition at the liquid-solid interface is expressed as the following:

$$T|_{y=h} = T_m \tag{29}$$

$$-\lambda_l \left.\frac{\partial T}{\partial y}\right|_{y=h^-} + \lambda_s \left.\frac{\partial T}{\partial y}\right|_{y=h^+} = L_m \rho_s \dot{r}_m \tag{30}$$

Finally, the ambient temperature T_a is imposed on the boundary domain deep in the solid grain.

The equations 19 and 20 must be solved on a dynamic mesh due to the liquid-layer thickness dynamics. For this reason, it is necessary to pay special attention to the mesh construction, the discretization of the convective flux term and the numerical time integration. The spatial discretization is obtained by using the finite volume method, where the diffusive flux term is discretized with a second-order central scheme and the convective flux term with the second-order upwind scheme through the minmod slope limiter. The time integration is performed with the second-order Runge-Kutta SSP (Strong Stability Preserving) [38]. The time integration scheme must consider the time-evolving grid deformation; consequently, it has followed the approach suggested in [39]. The mesh grid is discretized with 100 cells and the liquid layer is discretized with 20 cells. The grid nodes are uniformly spaced in the liquid layer; in the solid region, the grid nodes are distributed according to a geometric progression in order to achieve better resolution close to the liquid-solid interface. The extension of the domain in the solid region is $100\,\delta$, where $\delta = \frac{\alpha_s}{\dot{r}_{ref}}$ is the thermal thickness in the solid phase. A schematic diagram of the grid discretization performed on the fluid and solid domain is presented in Fig.1:

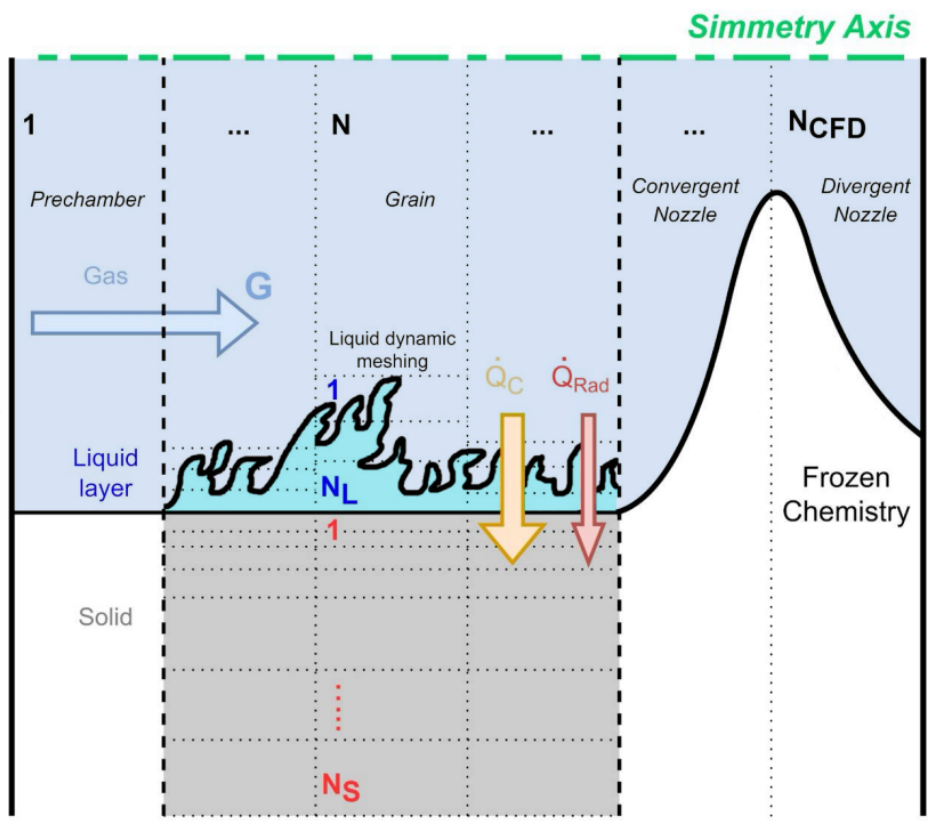

Fig. 1 Domain discretization

C. Convective Heat Flux Modelling

Assuming a fully developed turbulent boundary layer and the validity of the Reynolds analogy in the quasi-stationary condition, the following expression for the convective heat flux can be assumed [32]:

$$\dot{Q}_c = \frac{1}{2} C_f G \left(\frac{u_e}{u_b} \right) \Delta h \tag{31}$$

The convective heat flux through the boundary layer is limited by the blowing of the gasified fuel. This phenomenon is taken into account by the introduction of the aerodynamic blowing parameter evaluated as the following:

$$B = \frac{2\rho_F \dot{r}_v}{G C_f} \tag{32}$$

Note that, following Ref. [32], the vaporization of the fuel liquid particles detached from the melted layer is assumed to take place above the flame sheet and as a consequence, the evaporation regression rate appears in the above equation instead of the total regression rate. In the range $5 \geq B \geq 100$, the ratio between the skin friction coefficient affected by blowing C_f and the skin friction without blowing C_{f0} is expressed as in Ref. [40]:

$$\frac{C_f}{C_{f0}} = qB^{-k_b} \tag{33}$$

while, when $B \to 0$:

$$\frac{C_f}{C_{f0}} = \frac{1}{1+0.4B} \tag{34}$$

Following the approach suggested in Ref. [41, 42] it is assumed $k_b = 0.68$, $q = 0.996$ and $B_{ref} = 5.313$, where B_{ref} is the value of B for which Eq. 33 and Eq. 34 match. Note that at $B = B_{ref}$, both the function C_f/C_{f0} and its derivative are continuous. The skin friction coefficient without blowing C_{f0} is estimated according to the correlation reported in Ref.[32]:

$$\frac{C_{f0}}{2} = 0.03\left(\frac{G\,x}{\mu_g}\right)^{-0.2} \tag{35}$$

where G is the mass flux, x the axial coordinate along the grain and μ_g is the gas viscosity of paraffin fuel. Combining Eq.32 with Eq.33 and Eq.34, it is possible to determine two different expressions for the blowing parameter:

$$B = \frac{2\rho_F \dot{r}_v}{GC_{f0} - 0.8\rho_F \dot{r}_v} \tag{36}$$

$$B = \left(\frac{2\rho_F \dot{r}_v}{qGC_{f0}}\right)^{\frac{1}{1-k_b}} \tag{37}$$

Eventually, by taking into account the thermochemical blowing parameter $B_t = \left(\frac{u_e}{u_b}\right)\frac{\Delta h}{h_v}$, the following two expressions for the convective heat flux can be derived:

$$\dot{Q}_c = B_t h_v \left(\frac{1}{2}C_{f0}G - 0.4\rho_F \dot{r}_v\right) \quad \text{if} \quad B \leq B_{ref} \tag{38}$$

$$\dot{Q}_c = \frac{0.996}{2}C_{f0}B_t h_v \left(\frac{2\rho_F \dot{r}_v}{0.996GC_{f0}}\right)^{\frac{-k_b}{1-k_b}} \quad \text{if} \quad B > B_{ref} \tag{39}$$

In the code, B is firstly computed using Eq.36 and if the result of the computation is less than B_{ref} and greater than zero then that is the value of the blowing parameter, otherwise B is calculated using Eq.37.

D. Boundary Layer Delay Modelling

As stated in Ref. [43], combustion instability in HREs depends on at least three physical phenomena: the blocking-effect due to the blowing of the fuel gas, the thermal transient and the boundary layer delay time. The instability is triggered in the model by the boundary layer delay time value. This parameter can be estimated as a function of the Reynolds number according to [43]:

$$\tau_{bl} = 2.18 {Re_x}^{-0.1} \frac{x}{u_e} \tag{40}$$

This formulation is derived through the model of the flat plate. Another formulation, proposed in Ref. [14], is obtained by fitting experimental data in a wide range of fuels (including paraffin-based fuels), oxidizers, engine dimensions and operating conditions:

$$\tau_{bl} = 2.05 \left(\frac{x}{u_e} \right) \tag{41}$$

When the effect of boundary layer delay is considered, the convective heat flux at the grain surface is modified, in order to simulate the boundary layer dynamics, by using the evaporation regression rate calculated at $t - \tau_{bl}$ instant. Thus, Eq.38 and Eq.39 can be written as:

$$\dot{Q}_c = B_t h_v \left(\frac{1}{2} C_{f0} G - 0.4 \rho_F \dot{r}_v (t - \tau_{bl}) \right) \quad \text{if} \quad B \leq B_{ref} \tag{42}$$

$$\dot{Q}_c = \frac{0.996}{2} C_{f0} B_t h_v \left(\frac{2 \rho_F \dot{r}_v (t - \tau_{bl})}{0.996 G C_{f0}} \right)^{\frac{-k_b}{1-k_b}} \quad \text{if} \quad B > B_{ref} \tag{43}$$

Using the same approach, also Eq.36 and Eq.37 are computed taking into account the boundary delay term:

$$B = \frac{2 \rho_F \dot{r}_v (t - \tau_{bl})}{G C_{f0} - 0.8 \rho_F \dot{r}_v (t - \tau_{bl})} \tag{44}$$

$$B = \left(\frac{2 \rho_F \dot{r}_v (t - \tau_{bl})}{q G C_{f0}} \right)^{\frac{1}{1-k_b}} \tag{45}$$

E. Radiative Heat Flux

The boundary condition at the liquid-gas interface requires that the total heat flux is the sum of convective and radiative heat flux. The radiative heat transfer usually does not have a strong influence on the regression rate; it could become relevant when considering fuels with metal additives or sooting fuels. Empirical relations are available to the estimation of the radiative heat flux such as [13, 44]:

$$\dot{Q}_r = \sigma \epsilon_w \left(\epsilon_g {T_b}^4 - \alpha_g {T_w}^4 \right) \tag{46}$$

In this model a unit view factor is assumed: this assumption is valid for sufficiently high values of mass flux, as the view factor increases with the mass flux as the boundary layer becomes thinner and more optically thick [45]. Since the flame temperature is significantly higher than the surface temperature and, in addition, the gas phase emissivity and

absorptivity are of the same order, the equation for the radiative heat transfer can be approximated as the following:

$$\dot{Q}_r = \sigma \epsilon_w \epsilon_g {T_b}^4 \tag{47}$$

F. Swirl Model

The use of swirled injectors can significantly increase the regression rate by improving convective heat transfer. A detailed description of swirled flows in hybrid rockets is presented in Ref.[46–48]. In order to model the use of a swirl injector, an empirical correction based on a simplification is introduced. The gas dynamic model considered in this work is quasi-1D: this means that it can describe only the axial component of the velocity. In order to introduce the swirl effect, a correction factor is introduced on the gas velocity in order to keep into account the tangential velocity component. According to [49], the swirl number S_n is defined as

$$S_n = \frac{2}{3}\frac{v}{u} \tag{48}$$

where v and u represent the tangential and axial velocity components. The swirl correction factor K is computed as

$$K = \sqrt{1 + \left(\frac{3}{2}S_n\right)^2} \tag{49}$$

The factor K allows to correct the axial mass flux and speed by computing some equivalent values which take into account the swirl and allow to obtain an increased convective flux:

$$G_{swirl} = G \cdot K \tag{50}$$

In this strong approximation, S_n represents the average swirl number in the combustion chamber. Furthermore, in this approach the particles should move in a spiral trajectory: for this reason, the correction factor K is applied also to the space coordinate which appears in the empirical relation used to compute the skin friction coefficient C_f. As a result, also the characteristic boundary layer delay is corrected.

III. Chemical Model

In the combustion chamber of a HRE the characteristic time related to fluid dynamics phenomena is remarkably higher than the characteristic time associated to chemical reactions [14]. For this reason, it is reasonable to assume that the shifting equilibrium hypothesis holds. This assumption is in line with the approach proposed by Karthikeyan and Shimada in Ref. [28] and is here adopted.

In the present work, the chemical equilibrium is computed by means of two different models, namely a high fidelity

and a surrogate model. The High Fidelity Model (HFM), described in subsection A, is based on the NASA CEA code [50]. Such an approach, however, is really demanding in terms of computational time when embedded in the fluid dynamic solver which requires to compute the equilibrium composition in each cell at each time step. For this reason, Karthikeyan and Shimada [28] proposed to freeze the molar fractions of the chemical species for a certain number of time steps. Nevertheless, this approach is in contrast with the initial assumption concerning the characteristic times of fluid dynamics and chemical reactions. Hence, in the present work, the authors opt for the introduction of a surrogate chemical model, able to compute the chemical composition in each cell at each time step, but at an affordable computational cost. Such a surrogate model is depicted in Subsection B.

The evaluation of the chemical composition in equilibrium conditions is usually based on Gibbs' free energy minimization principle (when pressure and temperature of the reactions are given) or on Helmholtz's free energy minimization principle (when density and internal energy are given). In the present approach, the conservation principles employed in the gas-dynamic model describe the evolution of mass, momentum and energy. Thus, the chemical composition in equilibrium conditions can be easily computed minimizing Helmholtz free energy. For this reason, the inputs of the chemical model are density, internal energy and local mixture fraction ϵ. The outputs are the mole fractions of the combustion products and the isentropic exponent γ_s, which is related to the ratio of the specific heats γ as follows:

$$\gamma_s = -\frac{\gamma}{\left(\frac{\partial \ln V}{\partial \ln p}\right)_T} \tag{51}$$

and allows for the evaluation of the speed of sound [50]:

$$a = \sqrt{\gamma_s R T} \tag{52}$$

A. High Fidelity Model

The HFM assumes that all the gaseous chemical species present in the combustion chamber can be regarded as ideal gases and that their mixture follows the ideal gas equation as well. The chemical equilibrium problem is solved following the procedure proposed by McBride and Gordon, whose details can be found in Ref. [50]. In analogy to Ref. [28], only a selected number of gaseous species is considered to be present in the combustion gas in order to reduce computational costs. Following Ref. [12], it is here assumed that paraffin-based decomposes producing ethylene and hydrogen, i.e.:

$$C_{32}H_{66} \rightarrow 16\, C_2H_4 + H_2 \tag{53}$$

When the fuel is burning with Hydrogen Peroxide (HP), the following species are considered in the combustion gases: CO_2, C_2H_4, H, H_2, H_2O, O, OH, O_2 and H_2O_2. On the other hand, Ref. [28] proposes the following 8-species

selection when Gaseous Oxygen (GO_x) is used: CO_2, C_2H_4, H, H_2, H_2O, O, OH and O_2. In the present work, another chemical model with the addiction of CO has been proposed and analyzed for the GO_x case.

B. Surrogate Model

In order to reduce the computational cost required by the chemical equilibrium problem, an Artificial Neural Network (ANN) has been developed for both HP and GOX cases. The ANN requires three inputs, namely internal energy, density and local mixture ratio, whereas the output parameters are the molar fractions of the combustion products and γ_s. An example of the employed ANN architecture is reported in Fig. 2, where it is possible to identify the three inputs (on the left), two hidden layers of ten neurons each and the output layer of ten outputs (on the right). The architectures were chosen after a proper trade-off between prediction accuracy and training cost.

The ANN is trained in Matlab and embedded into a Fortran 90 code which solves the gas dynamic equations. The training database is generated by varying the input parameters in a given range defined after preliminary runs of the solver with the high-fidelity model. Initially, a uniform sampling was used for the generation of the training database with the high-fidelity model. However, some of these training points lead to unfeasible solutions (i.e. the high-fidelity model is unable to find a physical solution) and thus have been discarded from the training database. Moreover, for the GO_x case, the sampling of the training point has been crowded in regions of particular interest to achieve a better approximation of the results; this explains the denser regions in Fig.4.

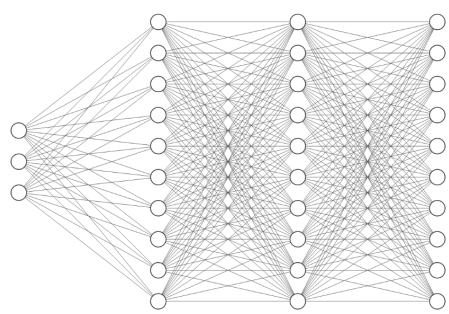

Fig. 2 ANN architecture used in the surrogate chemical model for HP.

The training has been performed, for both HP and GOX ANN, by means of the Levenberg-Marquardt algorithm, which aims at the minimization of the mean square error between the reference data set and the ANN reconstruction. The database is split into a training database (75% of the trials), a validation database (15% of the trials) and a test database (10% of the trials). The trials in the training database are used to determine the merit function (i.e. the mean square error on the fitting) which drives the training process. The validation trials are not used within the training but to stop it when the over-fitting issue kicks in. In the end, the test trials are not exploited during the training process but they are used a-posteriori to check the ANN prediction accuracy.

In order to further check the performance of the ANN, a large test database obtained by random sampling on the training range is considered. The results of this test for HP, with a training database made of 10^6 points, are shown in Fig. 3. The plot on the left reports the absolute error distribution, i.e. the value obtained by CEA minus the value

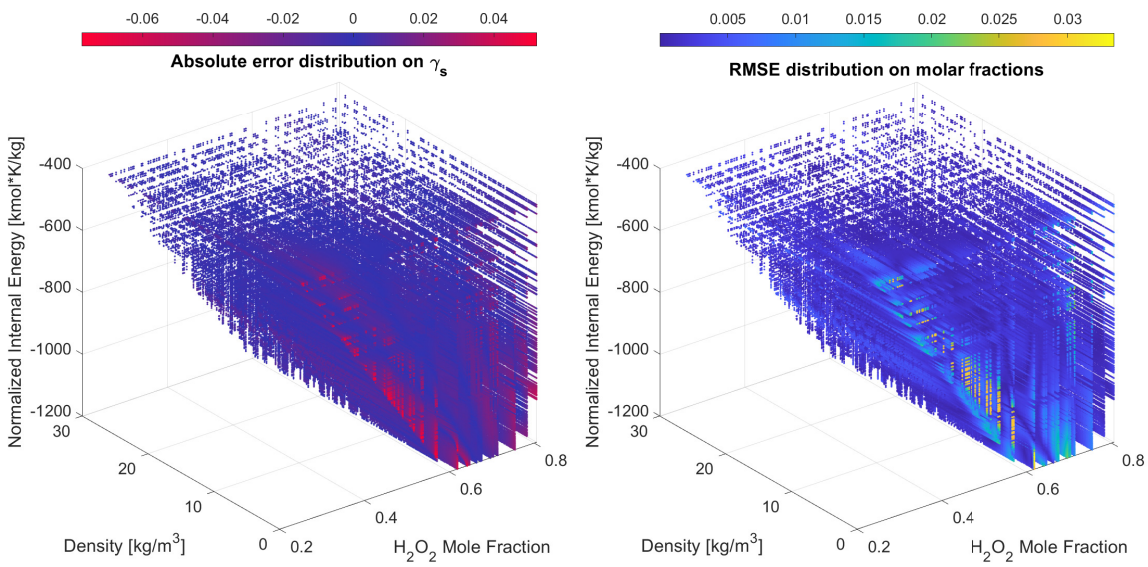

(a) (b)

Fig. 3 Absolute error distribution of γ_s (a) and RMSE of molar fractions (b) for HP.

predicted by the ANN, on the value of γ_s. In the same way, the plot on the right shows the root mean square error among all the products' molar fractions for each point of the database. The axes of both diagrams report the internal energy divided by the ideal gas constant, density and H_2O_2 mole fraction. The relative errors are smaller than 1% for both γ and the molar fractions, with the exception of the low-density region, which however is not relevant for the typical operating condition of the HREs considered in the present analysis (light blue and yellow points in Fig. 3, graph (b)). Moreover, the maximum absolute error is reported for every species in Tab.1 with the corresponding point of the map in which it occurs. In this way, it is immediate to see how both the error remains contained and the maximum error always occurs at the edges of the domain.

	Abs. Err.	H_2O_2 **Mole Fraction**	ρ $[kg/m^3]$	**e/**R_u $[kmol \cdot K/kg]$
γ_s	-0.0771	0.5341	0.010	-1057.9
CO_2	-0.0301	0.3533	0.010	-677.9
C_2H_4	-0.0465	0.2847	0.010	-438.5
H	0.0351	0.6419	0.010	-432.1
H_2	0.0666	0.6189	0.010	-1157.2
H_2O	-0.0727	0.6189	0.010	-1157.2
H_2O_2	0.0001	0.7827	29.06	-432.1
O	0.0071	0.8051	0.010	-432.1
OH	-0.0186	0.7134	0.010	-432.1
O_2	-0.0188	0.7543	0.010	-1130.1

Table 1 Maximum absolute error for every variable, HP

The ANN for GO_x, trained with a database of $2 \cdot 10^6$ points, is validated in a similar way and the same considerations made for HP also hold for GO_x, with the only difference that in this case the mixture fraction was used to train the ANN. The results of the validation are shown in Fig. 4 and Tab. 2. Similar results, not shown here, are obtained for the 8-species model.

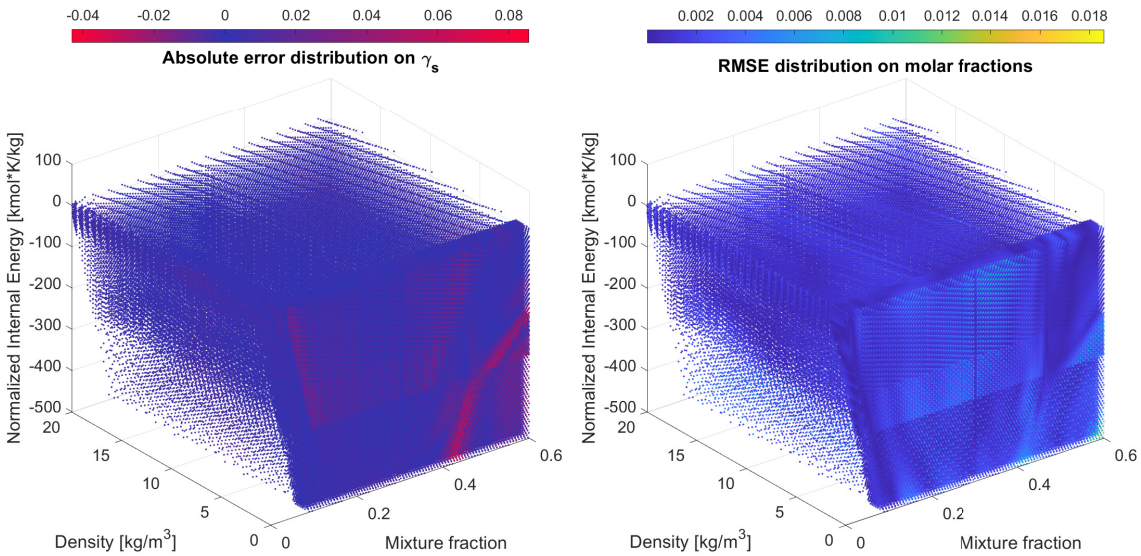

(a) (b)

Fig. 4 Absolute error distribution of γ_s (a) and RMSE of molar fractions (b) for GOX

	Abs. Err.	ϵ	ρ $[kg/m^3]$	**e/R_u** $[kmol \cdot K/kg]$
γ_s	0.0857	0.4520	0.045	-419.6
CO	0.0148	0.6000	0.045	-229.3
CO_2	0.0202	0.1838	20.000	-495.9
C_2H_4	0.0462	0.6000	14.924	-500.0
H	0.0228	0.3455	0.045	7.7
H_2	0.0369	0.4224	20.000	-500.0
H_2O	0.0310	0.3751	18.096	-500.0
O	0.0156	0.1529	0.045	7.7
OH	0.0067	0.2060	17.462	10.0
O_2	0.0163	0.1159	20.000	-495.9

Table 2 Maximum absolute error for every variable, GOX 9-species model.

Absolute errors are small with larger values occurring at the border of the domain of the training set of the ANN, a region of no practical interest for the present application.

One should note that, in contrast to HFM, the ANN model does not directly provide the mixture temperature. Then, it is necessary to impose that the internal energy provided by the gas-dynamic model and the internal energy predicted

using the ANN molar fractions are equal. A Newton-Raphson method can be exploited using equations 54, 55 and 56.

$$f\left(T_k\right) = \frac{e}{R_u} - \frac{h}{R_u} + \frac{T_k}{M} \tag{54}$$

$$f^{'}\left(T_k\right) = -\frac{c_p}{R_u} + \frac{1}{M} \tag{55}$$

$$T_{k+1} = T_k - \frac{f\left(T_k\right)}{f^{'}\left(T_k\right)} \tag{56}$$

Once the temperature is obtained is possible to calculate all the other thermodynamic variables. The proposed surrogate model has been used to replace the HFM, granting a relevant reduction of the computational cost.

IV. HP Oxidizer Results

In this section the results for HP oxidizer are presented. First, in subsection A a steady state case is considered to calibrate the model; then, in subsection B, the results of a sensitivity analysis, carried out to evaluate the influence of most relevant parameters on instability characteristics, are presented.

A. Steady Results

The model is calibrated in steady state conditions by using experimental data of an engine burning paraffin-based fuel and hydrogen peroxide (90% concentration) presented in Ref. [33]. The numerical steady state solution is obtained by setting $\tau_{bl} = 0$. Among the different configurations described in Ref. [33], the selected one is characterized by the largest O/F ratio: 4.03. It is important to remember that the regression rate measurements described in Ref.[33] could be affected by post-burn melting.

The computational domain considered in the gas dynamics module includes the pre-chamber ($0 \leq x/L_{ref} \leq 0.1$), the grain section ($0.1 \leq x/L_{ref} \leq 0.8$) and the nozzle ($x/L_{ref} > 0.8$). The domain ends after the nozzle throat in order to achieve supersonic exit boundary conditions. In all the figures presented in this work, the axial position is normalized with respect to the total length of the computational domain ($L_{ref} = 0.150$ m).

The port area and the pre-chamber area are set equal to the same value, obtained by considering the average port area during the combustion ($A_p = 1.25 \cdot 10^{-3} m^2$). The throat is located at $x/L_{ref} = 0.925$ and its area A_t is set equal to $7.125 \cdot 10^{-5} m^2$.

The calibration is performed by optimizing the values of the coefficients a_{ent} and A_h in order to match the experimental average regression rate. Starting from data available in the literature, the following values were determined: $a^*_{ent} = 1.26 \cdot 10^{-13} m^9/kg^3$, $A^*_h = 1.88 \cdot 10^7 m/s$. Radiative effects are not considered in this simulation. As a result, the average regression rate is obtained equal to 2.7 mm/s which matches the experimental reference value. Using the o/f and the pressure at the end of the grain is possible to evaluate how well the surrogate model performs. Using the

species described in Sec. III this code estimates a temperature of 2801 K, while the CEA, using a paraffin with the same properties as the one used in this code and no limitations on the number of species considered, predicts a temperature of 2778 K. Therefore, for the mixture ratio used in this test case the surrogate model offers a great level of approximation. However, if a test case with a lower mixture fraction had to be carried out, the addiction of CO in the surrogate model should be taken into consideration. The mixture fraction and regression rate distribution along the axis are reported in Figure 5. The mass flux and the chemical composition are reported in Figure 6. Density and temperature are reported in Figure 7. The liquid layer thickness and the grain temperature distribution are reported in Figure 8. Finally, the pressure distribution is reported in Figure 9.

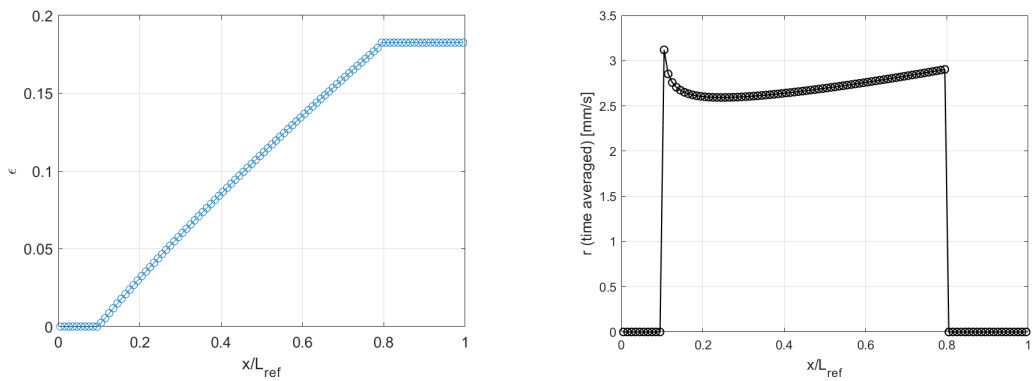

(a) (b)

Fig. 5 Mixture fraction ϵ (a) and regression rate r (b) along the grain axis for the steady solution.

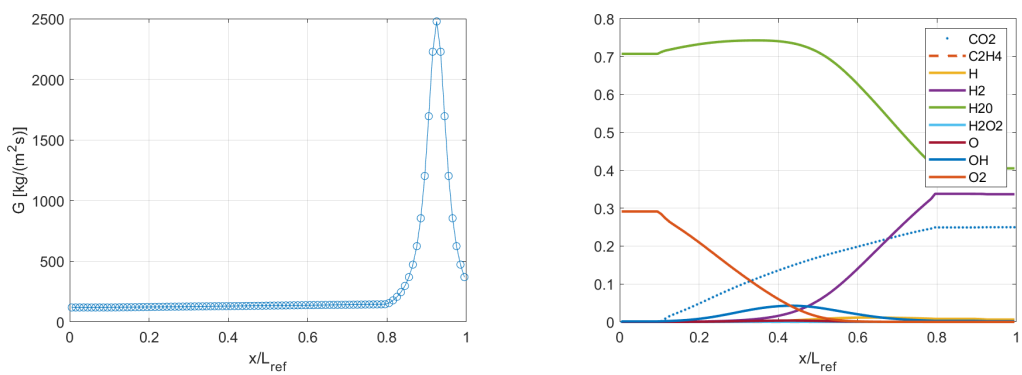

(a) (b)

Fig. 6 Mass flux G (a) and combustion products molar fractions (b) along the grain axis for the steady solution.

B. Parametric study for HP

The results obtained by the steady simulation (Case A, in the following) represent a baseline solution which will be considered as a reference in the following and compared with the other simulations which are summarized in Tab. 3.

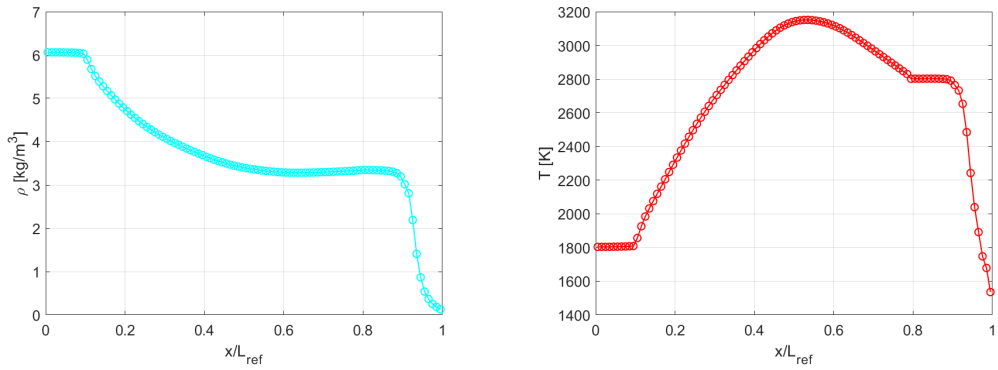

(a) (b)

Fig. 7 Density ρ (a) and temperature T (b) along the grain axis for the steady solution.

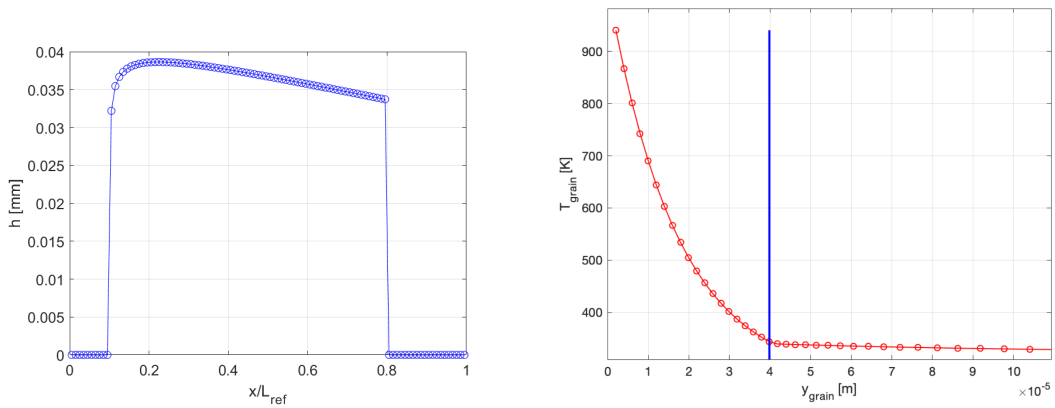

(a) (b)

Fig. 8 Liquid layer thickness h (a) along the grain axis and grain temperature T_{grain} (b) within the grain thickness for the steady solution.

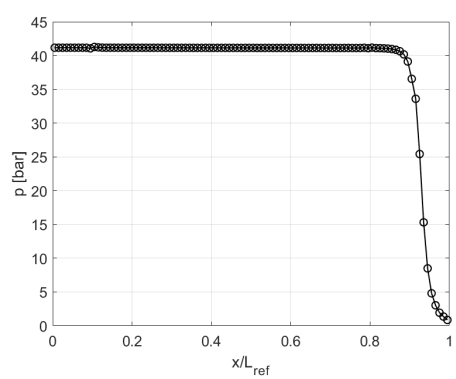

Fig. 9 Pressure p along the grain axis for the steady solution

In case B, a simulation is performed using a value of A_h that is half of the reference one: the result shows how the entrainment has the biggest impact on the regression rate, since halving the A_h coefficient has a very low impact on the regression rate, which decreases by only about 2%.

A set of unsteady simulations is performed in order to evaluate the effects of some model coefficients. This sensitivity analysis is focused on four target quantities: average chamber pressure $\bar{p}_c$, relative mean squared pressure fluctuation $\Delta p_2\%$, relative peak-to-peak pressure fluctuation $\Delta p_{pp}\%$ and average regression rate $\bar{r}$. The average quantities are obtained by performing time averaging on the statistically steady solution obtained after the initial transient. In particular, the impact of the following coefficients is investigated: boundary layer delay τ_{bl}, entrainment coefficient a_{ent}, Arrhenius pre-exponential coefficient A_h, overall radiative coefficient $\epsilon_g \epsilon_w$, swirl number S_n. The results of the unsteady simulations (C-K) and the corresponding set of coefficients are summarized in Tab. 3.

Case	τ_{bl}	a_{ent}	A_h	$\epsilon_g \epsilon_w$	S_n	$\bar{p}_c$ [bar]	$\Delta p_2\%$	$\Delta p_{pp}\%$	$\bar{r}$ [mm/s]
A	0	a^*_{ent}	A^*_h	0.00	0.00	41.15	/	/	2.71
B	0	a^*_{ent}	$0.5A^*_h$	0.00	0.00	41.05	/	/	2.66
C	$\tau_{bl}(x) = 5$ ms	a^*_{ent}	A^*_h	0.00	0.00	42.10	1.35	9.58	3.29
D	$\tau_{bl} = 2.18\, Re_x{}^{-0.1} \left(\frac{x}{u_e}\right)$	a^*_{ent}	A^*_h	0.00	0.00	42.21	0.87	5.64	3.30
E	$\tau_{bl} = 2.18\, Re_x{}^{-0.1} \left(\frac{x}{u_e}\right)$	0	A^*_h	0.00	0.00	38.97	3.97	23.38	1.97
F	$\tau_{bl} = 2.18\, Re_x{}^{-0.1} \left(\frac{x}{u_e}\right)$	$0.25a^*_{ent}$	A^*_h	0.00	0.00	41.06	2.46	12.66	2.59
G	$\tau_{bl} = 2.18\, Re_x{}^{-0.1} \left(\frac{x}{u_e}\right)$	$0.5a^*_{ent}$	A^*_h	0.00	0.00	41.38	1.86	8.95	2.66
H	$\tau_{bl} = 2.18\, Re_x{}^{-0.1} \left(\frac{x}{u_e}\right)$	$2a^*_{ent}$	A^*_h	0.00	0.00	42.74	0.61	4.02	3.85
I	$\tau_{bl} = 2.18\, Re_x{}^{-0.1} \left(\frac{x}{u_e}\right)$	a^*_{ent}	$2A^*_h$	0.00	0.00	42.34	0.90	6.55	3.42
J	$\tau_{bl} = 2.18\, Re_x{}^{-0.1} \left(\frac{x}{u_e}\right)$	a^*_{ent}	A^*_h	0.04	0.00	42.29	0.89	6.05	3.37
K	$\tau_{bl} = 2.18\, Re_x{}^{-0.1} \left(\frac{x}{u_e}\right)$	a^*_{ent}	A^*_h	0.00	1.00	47.71	0.49	3.18	6.22

Table 3 HP sensitivity analysis.

Then, simulations are performed considering the presence of the boundary delay term τ_{bl}. First of all, an unsteady simulation with a uniform boundary layer delay (Case C) is performed ($\tau_{bl} = 5$ ms). This value was arbitrarily chosen to perform a preliminary check on the implementation. The obtained pressure spectrum is reported in Fig. 10. The first peak is in good agreement with the fundamental hybrid frequency predicted according to the Karabeyoglu correlation [43], $f = 0.48/\tau_{bl} = 96$ Hz. It is interesting to note that the instability induces a significant increase in the average chamber pressure and regression rate (DC shift phenomenon).

All the other simulations are performed by imposing an axial distribution of $\tau_{bl} = f(x)$ obtained by applying Eq. 40 to the previously computed steady-state solution. A plot of this distribution is reported in Fig. 11. This is a better approximation with respect to the imposition of a uniform boundary layer delay. Ideally, it could be possible to apply Eq. 40 at run-time in the unsteady simulation in order to get a delay which varies both in space and in time, according to the local state of the boundary layer. However, Eq. 40 is valid only for a steady solution and its application to the unsteady solution could lead to nonphysical results, for example when the flow inverts its direction during the strong initial transient. The pressure spectrum obtained by setting $\tau_{bl} = 2.18\, Re_x{}^{-0.1} \left(\frac{x}{u_e}\right)$ and keeping the original values for

all the other coefficients (Case D) is reported in Fig. 10b: it is no more possible to identify a clear set of peaks because in this simulation the boundary layer delay varies continuously along the axial direction. Also in this case it is possible to observe a significant DC shift: the magnitude of DC shift seems to be overestimated with respect to results available in the literature [42].This point will be further investigated in future works.

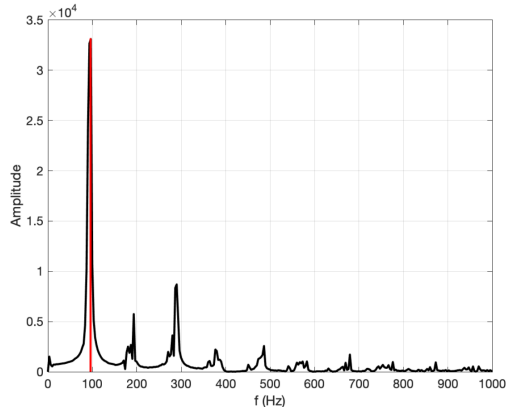

Fig. 10 Pressure spectrum for unsteady combustion with uniform boundary layer delay (τ_{bl}=5 ms).

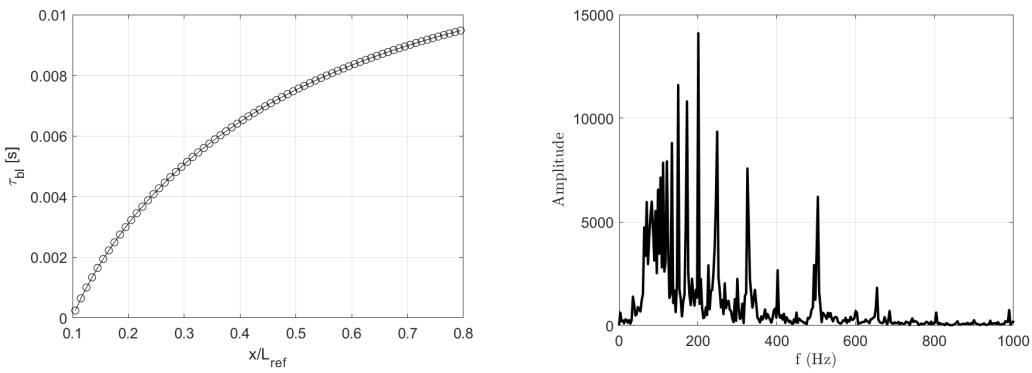

(a) (b)

Fig. 11 Boundary layer delay estimated from the steady solution (a) and pressure spectrum (b) obtained by imposing this delay distribution.

In Cases E, F and G the effect of decreasing the a_{ent} coefficient with respect to the calibration (a^*_{ent}) is evaluated. It is immediate to notice the huge effect that a_{ent} bears on the regression rate, increasing it. Moreover, lowering the a_{ent} coefficient increases the pressure instabilities.

In Case H, the effect of entrainment is investigated by doubling the coefficient a_{ent} with respect to the value obtained by the calibration (a^*_{ent}). As a result, the average regression rate and chamber pressure are increased with respect to case D. Furthermore, the increased entrainment leads to some benefits on the combustion instability: both Δp_2% and Δp_{pp}% are reduced with respect to the Case D.

In case I, the effect of vaporization and pyrolysis is investigated by doubling the Arrhenius coefficient A_h with

respect to the value obtained by the calibration (A_h^*). Also in this case, the average regression rate and chamber pressure are increased with respect to Case D. However, the pressure oscillations, quantified by the coefficients $\Delta p_2\%$ and $\Delta p_{pp}\%$ remain comparable to what observed in Case D.

In Case J, the effect of radiative fluxes is evaluated by setting the overall radiative coefficient as $\epsilon_g \epsilon_w = 0.04$. This tentative value was chosen after some tests in order to keep the radiative flux below 10% of the convective flux, as reported in the literature [13]. The results show that the radiative flux leads to a *small* increase in the average regression rate, chamber pressure and pressure fluctuations with respect to Case D.

Finally, in case K the effects of swirl injection are estimated. In particular, the swirl number is set to $S_n = 1$. This leads to a strong increase in the average regression rate and chamber pressure. Furthermore, the swirl has an important effect on the instability: both $\Delta p_2\%$ and $\Delta p_{pp}\%$ are significantly reduced with respect to Case D.

V. GOX Oxidizer Results

As for HP, a preliminary steady simulation is carried out in order to further validate the code. Moreover, the steady solution is used to assess the best chemical model between the one proposed by Karthikeyan and Shimada [28] and the one with the addition of CO. Then, with the activation of the boundary layer delay term, an unsteady simulation is performed to better understand the relationship between the instability characteristics and the model shape of the boundary layer delay.

A. Steady Results

The steady solution is obtained imposing τ_{bl} equal to zero. The motor data for the simulation are obtained by one of the test cases performed by Karabeyoglu et al. at NASA Ames Research Center [16]; more precisely the reference test case is test N. 12, whose characteristics are reported in Tab. 4.

GOX Reference Test Summary	
Initial Port Internal Diameter $[mm]$	24.0
Final Port Internal Diameter $[mm]$	31.8
Oxidizer Flow rate $[g/s]$	26.1
O/F	1.34
Regression Rate $[mm/s]$	1.293
Average Oxidizer Flux $[g/(cm^2 \cdot s)]$	4.3
Chamber Pressure $[atm]$	7
Grain Length $[cm]$	17.10
Burn Time $[s]$	3.0
Nozzle Throat Internal Diameter $[mm]$	9.14
Fuel Mass Burned $[g]$	58.4

Table 4 Summary of Karabeyoglu et al. test 12 [16].

As for HP, chamber axial positions are normalized with respect to the total length of the computational domain $(L_{ref} = 0.244\ m)$. In this way, the definitions of pre-chamber, grain section and nozzle are equal to the ones made for HP in Section IV. The values of the coefficients a_{ent} and A_h are found through an iterative process with the aim to obtain the same regression rate experienced in the reference test case; with the values of $a_{ent} = 2.585 \cdot 10^{-13}\ m^9/kg^3$ and $A_h = 18.4194 \cdot 10^6\ m/s$ the average regression rate obtained in the simulation is equal to 1.294 mm/s, a value very close to the 1.293 mm/s obtained by Karabeyoglu et al. [16], and a mixture ratio of 1.44 is calculated at the end of the propellant grain. In Fig. 12 the molar fractions provided by the code for the 8 and 9 species models are shown.

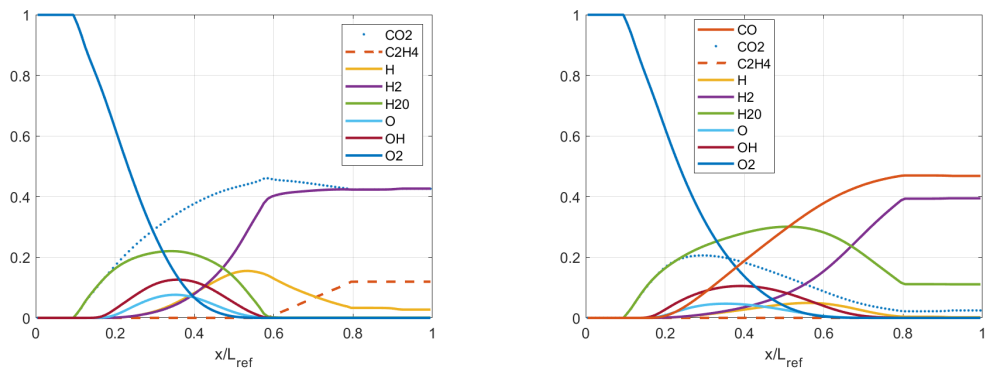

(a) (b)

Fig. 12 Comparison of molar fractions between 8 (a) and 9 (b) species models.

It is immediate to observe some significant differences between the two models:

- Soon after the section at $x/L_{ref} = 0.2$, the 9-species model predicts formation of CO and a reduction of CO_2 molar fraction;
- In the 8-species model, after the section at $x/L_{ref} = 0.6$ there is no more oxygen left to complete the combustion reaction: ethylene molar fraction grows until the end of the grain.
- In the 9-species model, all the ethylene is oxidized forming CO and H_2O. The H_2O molar fraction is larger with respect to the 8-species model.

In Fig. 13 and Fig. 14 are shown the temperature and pressure profile along the chamber for the two models. The pressure distribution shows a spike between prechamber and grain: this is due to a discretization error caused by a discontinuity in the source term of Eq.1, . However, this discretization error diminishes as the mesh is refined and so the discretization remains consistent.

There are two main differences between the two models:

- The maximum temperature in the chamber is 3796 K for the 8-species model and 3463 K for the 9-species one.
- The temperature at the end of the grain is 2470 K for the 9-species model, while for the 8-species model this value is equal to 3015 K.

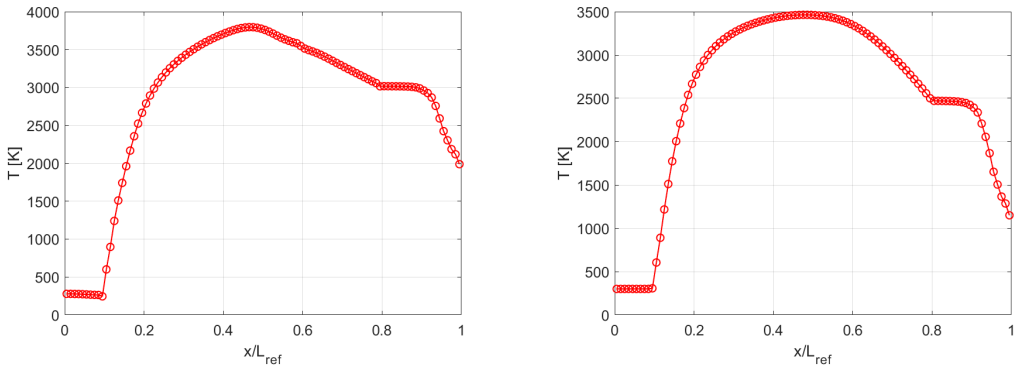

(a) (b)

Fig. 13 Temperature T profile comparison between 8 (a) and 9 (b) species models.

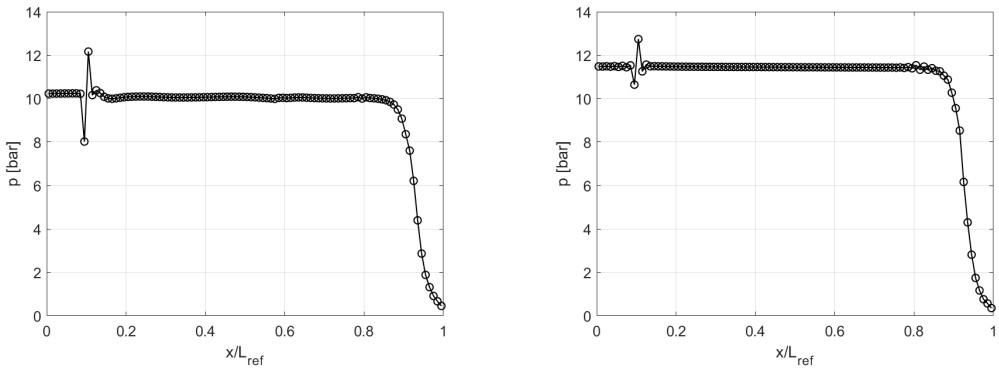

(a) (b)

Fig. 14 Pressure p profile comparison between 8 (a) and 9 (b) species models.

The aforementioned results are compared to results obtained using all the available species and a paraffin with the same properties of the one used in this code in CEA for this test case, i.e. $p = 10\,bar$, $o/f = (1-\epsilon)/\epsilon = 1.454$ for 8-species model and $p = 11.45\,bar$, $o/f = (1-\epsilon)/\epsilon = 1.442$ for the 9-species model. Under these conditions, CEA predicts a temperature of 2493 K with the output of the 8-species test case and a temperature of 2469 K for the 9-species one, showing that the 8-species model is to be discarded in favor of the 9-species model. Furthermore, a check is performed on the maximum temperature; CEA predicts, without any limitation on the species considered, a maximum temperature of 3466 K, further validating the 9-species model.

Moreover, the results obtained by the ANN were compared to the open-source chemical library Cantera [51], in addition to CEA. Using the same limitation on species, there are practically no differences between the output of the ANN and the two software. However, the ANN is a lot faster than both the CEA and Cantera, the latter using "The method of Element Potentials" [52] which is less demanding than the method used by CEA. In this way, is possible to confirm the ANN as the fastest tool to compute chemical equilibrium in the combustion chamber. Finally, the other

simulation results obtained are shown in the next figures, only for the 9-species model.

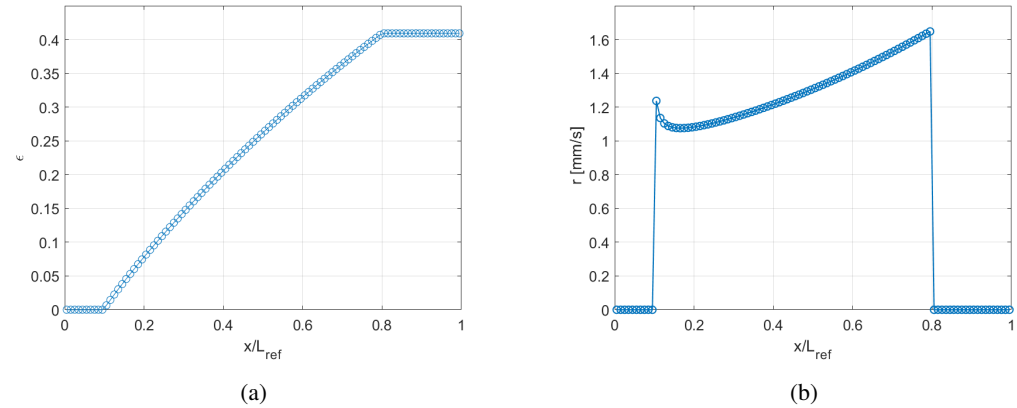

Fig. 15 Mixture fraction ϵ (a) and regression rate r (b) along the grain axis for the steady solution.

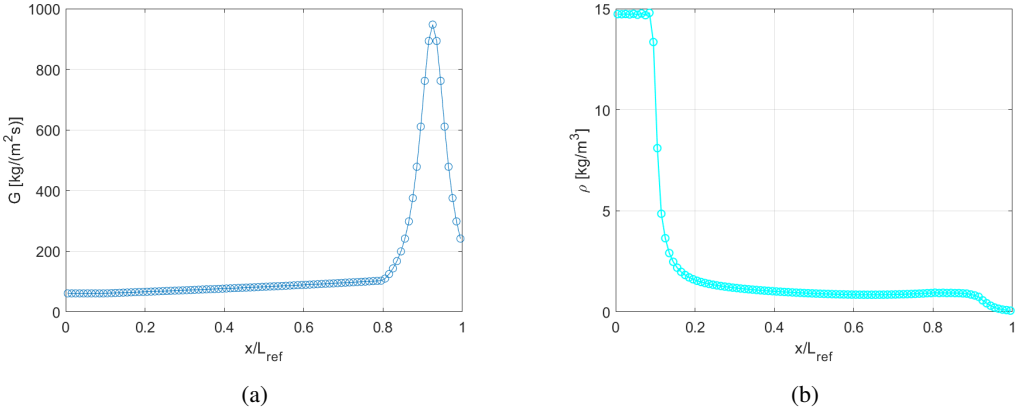

Fig. 16 Mass flux G (a) and density ρ (b) along the grain axis for the steady solution.

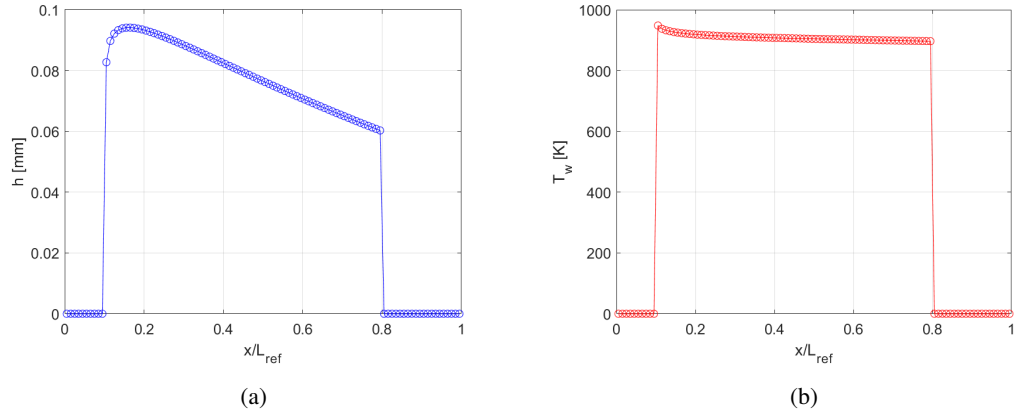

Fig. 17 Liquid layer thickness h (a) and grain temperature at the wall T_w (b) along the grain axis for the steady solution.

B. Parametric study for GOx

In case A, the results of the steady simulation are reported to provide a baseline solution. The mixture fraction and regression rate distributions are reported in Figure 15. Mass flux and density distributions are reported in Figure 16 while the liquid layer thickness and grain temperature are reported in Figure 17. Similarly to what happens for HP, case B shows how halving the A_h coefficient has very little effect on both the regression rate and pressure at steady conditions. Once the chemical model is validated, the unsteady solution is obtained activating the boundary layer delay term τ_{bl}. First, a constant delay term is used in order to check the behaviour of the code. The delay value is arbitrarily chosen since the purpose of this test is just to perform a simple verification of the model implementation. In fact, in the case of constant delay, it is possible to precisely predict the frequency peak in the instability spectrum using the relation $f = 0.48/\tau_{bl}$. Then, two distributions of τ_{bl} along the grain are compared with the aim of further assessing the effects of the delay term shape on the instability frequency. Finally, a radiative term is added to the simulation to evaluate its effect on the instability features and the mean regression rate. Similarly to the HP case, with the exception of the swirl that is not considered in the G_{OX} simulations, the following variables are analyzed: overall radiative coefficient $\epsilon_g \epsilon_w$, average chamber pressure $\bar{p}_c$, relative mean squared pressure fluctuation $\Delta p_2\%$, relative peak-to-peak pressure fluctuation $\Delta p_{pp}\%$ and average regression rate $\bar{r}$. The average quantities are obtained by performing time averaging on the statistically steady solution obtained after the initial transient. The results of the unsteady simulations (C-K) are summarized in Tab. 5.

Case	τ_{bl}	a_{ent}	A_h	$\epsilon_g \epsilon_w$	Sn	$\overline{p}_c$ [bar]	$\Delta p_2\%$	$\Delta p_{pp}\%$	$\bar{r}$ [mm/s]
A	0	a^*_{ent}	A^*_h	0	0	11.45	/	/	1.29
B	0	a^*_{ent}	$0.5A^*_h$	0	0	11.47	/	/	1.27
C	$\tau_{bl} = 12\,ms$	a^*_{ent}	A^*_h	0	0	10.88	7.5	34.6	1.89
D	$\tau_{bl} = 2.18\,Re_x{}^{-0.1}\left(\frac{x}{u_e}\right)$	a^*_{ent}	A^*_h	0	0	11.07	5.6	23.9	1.59
E	$\tau_{bl} = 2.05\left(\frac{x}{u_e}\right)$	a^*_{ent}	A^*_h	0	0	10.91	7.3	33.6	1.82
F	$\tau_{bl} = 2.05\left(\frac{x}{u_e}\right)$	0	A^*_h	0	0	10.40	10.48	68.38	0.99
G	$\tau_{bl} = 2.05\left(\frac{x}{u_e}\right)$	$0.25a^*_{ent}$	A^*_h	0	0	11.22	6.23	34.86	1.30
H	$\tau_{bl} = 2.05\left(\frac{x}{u_e}\right)$	$0.5a^*_{ent}$	A^*_h	0	0	11.26	6.17	32.9	1.44
I	$\tau_{bl} = 2.05\left(\frac{x}{u_e}\right)$	a^*_{ent}	$2A^*_h$	0	0	10.87	7.6	32.2	1.90
J	$\tau_{bl} = 2.05\left(\frac{x}{u_e}\right)$	$2a^*_{ent}$	A^*_h	0	0	10.71	7.7	27.3	2.37
K	$\tau_{bl} = 2.05\left(\frac{x}{u_e}\right)$	a^*_{ent}	A^*_h	0.04	0	10.88	7.5	34.6	1.89

Table 5 GOX sensitivity analysis.

In case C, the introduction of a constant delay term shows the onset of instability and of the DC shift phenomenon,

i.e. the rise of the mean regression rate. As in all the other simulations, the introduction of a boundary layer delay term has a very low effect on the mean pressure, for this motor configuration. This simulation can be used to verify the correct behaviour of the code before introducing the delay term as a function of the grain axial position; in fact, looking to Fig. 18, it is possible to see that the solution meets the expected instability peak with good approximation.

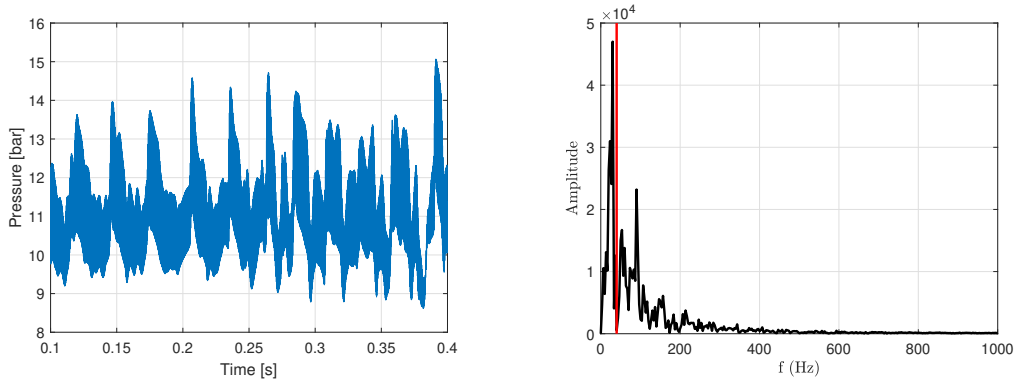

(a) (b)

Fig. 18 Pressure profile over time (a) and pressure spectrum (b) for constant boundary layer delay time. In graph (b) red line indicates the expected instability peak.

In case D, the boundary layer delay dependent on the Reynolds number is used. It is immediate to observe from Tab. 5 how this distribution also onsets both the instability and the DC shift. The boundary layer delay profile and the pressure spectrum are shown in Fig. 19. The pressure spectrum is characterized by frequency peaks at frequencies too high to be considered low-frequency instabilities [14].

A new law for the delay term, provided by Karabeyoglu through the interpolation of hybrid motor test data [14], is tested in case E and shown in Fig. 20. In this case, it is possible to see how the frequency peaks occur at lower frequencies. This shows a correlation that was already suggested by equation $f = 0.48/\tau_{bl}$, i.e. the frequency peaks occur at lower frequencies if the delay term grows higher. In fact, a comparison between cases D and E exhibits that a bigger mean delay value (3.8 vs 11.8 ms) corresponds to more pronounced instability features and a bigger increase in regression rate. Nevertheless, the mean value of the delay proves not to be sufficient to explain the phenomenon of instability, as a comparison between solutions C and E highlights completely different instability characteristics, despite the average value being similar. Furthermore, it should be noted that in Ref.[14] Karabeyoglu et al. show sharper experimental spectra for GOX/paraffin motor tests. The difference between the output of this work and experimental results could be related to the fact that in our model the boundary layer delay is set independently in each axial position and axial heat conduction is neglected in the grain: this approximation could hide interactions along the axial direction between contiguous points in the grain. These considerations should be also applied to the HP simulations.

In cases F, G and H the effect of decreasing the a_{ent} coefficient with respect to the calibration (a^*_{ent}) is assessed. As for Hp, it is clear that lowering the a_{ent} coefficient results in lowering the regression rate. However, unlike what happens

for HP, the effect of a_{ent} on pressure instability is evident only for the case $a_{ent} = 0$ (Case F), in which both Δp_2 and Δp_{pp} rise, while in case G and H there is little effect on pressure fluctuations.

In cases I and J a sensitivity analysis is performed doubling the vaporization and entrainment coefficient, respectively. As expected, doubling the vaporization coefficient and the entrainment coefficient from the calibrated values, respectively A_h^* and a_{ent}^*, results in an increase of the mean regression rate, with the entrainment coefficient having a bigger impact. Moreover, doubling the vaporization and entrainment coefficients results in a slight increase of Δp_2 and in a decrease of Δp_{pp}, with the entrainment coefficient having a bigger impact also on the instability features. These results show a good level of agreement with the HP results.

Finally, case K indicates that the radiative term has a small effect on the regression rate, increasing it, but has nearly no effect on the instability features Δp_2 and Δp_{pp}.

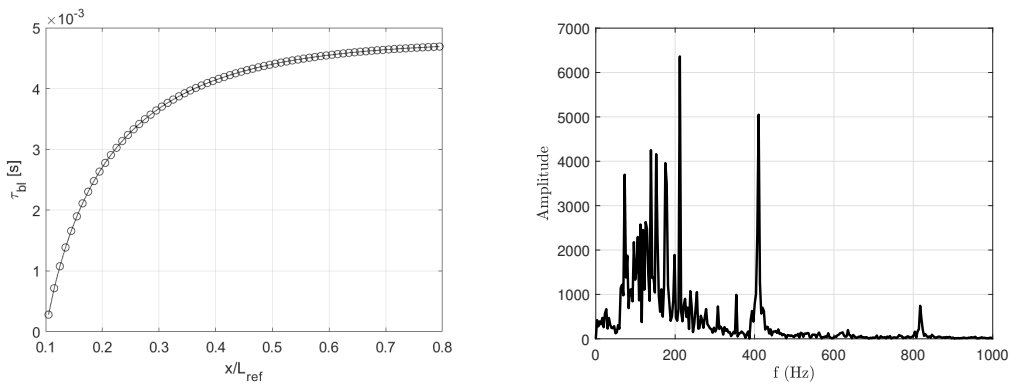

(a) (b)

Fig. 19 Boundary layer delay profile (a) and pressure spectrum (b) in the case of $\tau_{\mathbf{bl}} = 2.18\,\mathrm{Re_x}^{-0.1}\left(\frac{\mathbf{x}}{\mathbf{u_e}}\right)$.

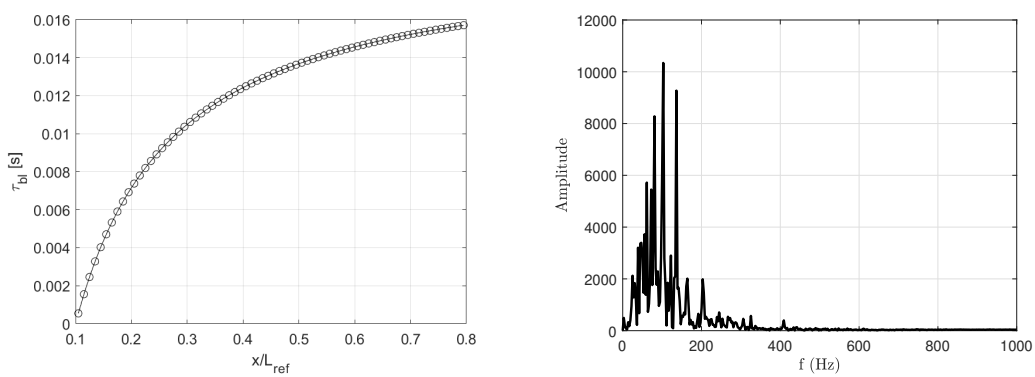

(a) (b)

Fig. 20 Boundary layer delay profile (a) and pressure spectrum (b) in the case of $\tau_{\mathbf{bl}} = 2.05\left(\frac{\mathbf{x}}{\mathbf{u_e}}\right)$.

VI. Conclusions

A multi-physics model for the prediction of the unsteady flow field in a HRE with liquefying fuel is presented. The model has a relatively low computational cost since it is based on a quasi-1D Euler solver coupled with a 1D thermal solver. In order to further reduce the computational cost, a surrogate model based on an ANN is adopted to compute the equilibrium chemical composition. As a result, the model can be adopted in the design process of a HRE in order to identify the risk of instability. The complexity of the involved physical phenomena requires severe simplifications in several problems which are approximated by empirical relations. This introduces a significant uncertainty on the predicted results and on the definition of the model parameters. For this reason, a sensitivity analysis was performed in order to identify the impact of some key parameters on regression rate and instability. The parametric study provides some guidelines which can be adopted during the design process. In particular, the results show that an increase in the entrainment phenomenon increases the regression rate but has a beneficial effect on the instability. This suggests the use of paraffin-based fuel with a reduced amount of additives in order to maximize the entrainment phenomenon: however, it is necessary to also take into account the mechanical properties of the fuel grain, which are not considered in this work and which can benefit from the introduction of additives in the composition.

Furthermore, a simple empirical correction for the presence of a swirled flow is introduced: the results suggest that the swirl allows to significantly increase the regression rate while limiting the combustion instability. This numerical result is in line with previous experimental findings reported by Ref. [53].

Finally, the results highlight the utmost importance of finding an appropriate boundary layer delay profile formulation to correctly modelize and evaluate a hybrid motor combustion chamber's instabilities.

VII. Acknowledgment

This work is performed under the funding of the Italian Space Agency contract n. 2019-5-I.0 CUP n. F84E16002240003 related to R&D on hybrid propulsion.

References

[1] Pastrone, D., "Approaches to low fuel regression rate in hybrid rocket engines," *International Journal of Aerospace Engineering*, Vol. 2012, 2012. doi:https://doi.org/10.1155/2012/649753.

[2] Karabeyoglu, M., Altman, D., and Cantwell, B., "Combustion of Liquefying Hybrid Propellants: Part 1, General Theory," *Journal of Propulsion and Power*, Vol. 18, No. 3, 2002, pp. 610–620. doi:10.2514/2.5975.

[3] Karabeyoglu, A., Zilliac, G., Cantwell, B. J., DeZilwa, S., and Castellucci, P., "Scale-up Tests of High Regression Rate Paraffin-based Hybrid Rocket Fuels," *Journal of propulsion and power*, Vol. 20, No. 6, 2004, pp. 1037–1045. doi:10.2514/1.3340.

[4] Karabeyoglu, M., and Cantwell, B. J., "Combustion of Liquefying Hybrid Propellants: Part 2, Stability of Liquid Films," *Journal of Propulsion and Power*, Vol. 18, No. 3, 2002, pp. 621–630. doi:10.2514/2.5976.

[5] Paravan, C., Galfetti, L., Bisin, R., and Piscaglia, F., "Combustion Processes in Hybrid Rockets," *International Journal of Energetic Materials and Chemical Propulsion*, Vol. 18, No. 3, 2019. doi:10.1615/IntJEnergeticMaterialsChemProp.2019027834.

[6] Bouziane, M., Bertoldi, A., Hendrick, P., and Lefebvre, M., "Experimental Investigation of the Axial Oxidizer Injectors Geometry on a 1-kN Paraffin-Fueled Hybrid Rocket Motor," *FirePhysChem*, 2021. doi:10.1016/j.fpc.2021.11.012.

[7] Thomas, J. C., Paravan, C., Stahl, J. M., Tykol, A. J., Rodriguez, F. A., Galfetti, L., and Petersen, E. L., "Experimental Evaluation of HTPB/paraffin Fuel Blends for Hybrid Rocket Applications," *Combustion and Flame*, Vol. 229, 2021, p. 111386. doi:10.1016/j.combustflame.2021.02.032.

[8] Paravan, C., Galfetti, L., and Maggi, F., *A Critical Analysis of Paraffin-based Fuel Formulations for Hybrid Rocket Propulsion*, 2017. doi:10.2514/6.2017-4830, URL `https://arc.aiaa.org/doi/abs/10.2514/6.2017-4830`.

[9] Bellomo, N., Barato, F., Faenza, M., Lazzarin, M., Bettella, A., and Pavarin, D., "Numerical and Experimental Investigation of Unidirectional Vortex Injection in Hybrid Rocket Engines," *Journal of Propulsion and Power*, Vol. 29, No. 5, 2013, pp. 1097–1113. doi:10.2514/1.B34506.

[10] Ranuzzi, G., Cardillo, D., and Invigorito, M., "Numerical Investigation of a N2O-paraffin Hybrid Rocket Engine Combusting Flowfield," *6th european conference for aeronautics and space sciences (EUCASS)*, EUCASS Rhode-St-Genese, Belgium, 2015. doi:10.13140/RG.2.1.1329.6727.

[11] Lazzarin, M., Faenza, M., Barato, F., Bellomo, N., Bettella, A., and Pavarin, D., "Computational Fluid Dynamics Simulation of Hybrid Rockets of Different Scales," *Journal of Propulsion and Power*, Vol. 31, No. 5, 2015, pp. 1458–1469. doi: 10.2514/1.B35528.

[12] Leccese, G., Bianchi, D., and Nasuti, F., "Modeling and Simulation of Paraffin–Based Hybrid Rocket Internal Ballistics," *2018 Joint Propulsion Conference*, American Institute of Aeronautics and Astronautics, Cincinnati, Ohio, 2018. doi: 10.2514/6.2018-4533.

[13] Kuo, K. K., and Chiaverini, M. J., *Fundamentals of Hybrid Rocket Combustion and Propulsion*, American Institute of Aeronautics and Astronautics, 2007. doi:10.2514/4.866876.

[14] Karabeyoglu, A., "Combustion Instability and Transient Behavior in Hybrid Rocket Motors," *Fundamentals of hybrid rocket combustion and Propulsion*, edited by M. J. Chiaverini and K. K. Kuo, American Institute of Aeronautics and Astronautics, Reston, Va, 2000, pp. 351–411. doi:10.2514/5.9781600866876.0351.0412.

[15] Boardman, T., Brinton, D., Carpenter, R., and Zoladz, T., "An experimental investigation of pressure oscillations and their suppression in subscale hybrid rocket motors," *31st Joint Propulsion Conference and Exhibit*, 1995. doi:10.2514/6.1995-2689.

[16] Karabeyoglu, A., Cantwell, B., and Stevens, J., "Evaluation of the Homologous Series of Normal Alkanes as Hybrid Rocket Fuels," *41st AIAA/ASME/SAE/ASEE Joint Propulsion Conference & Exhibit*, 2005, p. 3908. doi:10.2514/6.2005-3908.

[17] Park, K.-S., and Lee, C., "Low frequency instability in laboratory-scale hybrid rocket motors," *Aerospace science and technology*, Vol. 42, 2015, pp. 148–157. doi:10.1016/j.ast.2015.01.013.

[18] Rocker, M., *Modeling of Nonacoustic Combustion Instability in Simulations of Hybrid Motor Tests*, NASA/TP-2000-209905, Marshall Space Flight Center, 2000.

[19] Greatrix, D. R., "LF and HF Combustion Instability in Hybrid Rocket Engines," *2018 Joint Propulsion Conference*, 2018. doi:10.2514/6.2018-4527, URL `https://arc.aiaa.org/doi/abs/10.2514/6.2018-4527`.

[20] Uddanti, N. S., "Spatial Temporal Modeling of a Hybrid Rocket to Study Low Frequency Combustion Instabilities," *AIAA Propulsion and Energy 2020 Forum*, 2020. doi:10.2514/6.2020-3761.

[21] Dequick, B., Lefebvre, M., and Hendrick, P., "Two-Phase CFD Simulation of a 1kN Paraffin-Fueled Hybrid Rocket Motor," *AIAA Propulsion and Energy 2021 Forum*, 2021. doi:10.2514/6.2021-3493.

[22] Messinger, T. L., Hill, C. D., Quinn, D. T., and Johansen, C. T., "Hybrid Rocket Engine Performance Assessment Using Plume Luminosity Oscillations," *Journal of Propulsion and Power*, Vol. 38, No. 2, 2022, pp. 274–281. doi:10.2514/1.B38330, URL `https://doi.org/10.2514/1.B38330`.

[23] Migliorino, M. T., Bianchi, D., and Nasuti, F., "Numerical Analysis of Paraffin-Wax/Oxygen Hybrid Rocket Engines," *Journal of Propulsion and Power*, Vol. 36, No. 6, 2020, pp. 806–819. doi:10.2514/1.B37914, URL `https://doi.org/10.2514/1.B37914`.

[24] Migliorino, M. T., Bianchi, D., and Nasuti, F., "Numerical Simulations of the Internal Ballistics of Paraffin–Oxygen Hybrid Rockets at Different Scales," *Aerospace*, Vol. 8, No. 8, 2021. doi:10.3390/aerospace8080213, URL `https://www.mdpi.com/2226-4310/8/8/213`.

[25] Martino, G. D. D., Gallo, G., Mungiguerra, S., Carmicino, C., Savino, R., Cardillo, D., and Battista, F., *Recent advancements in experimental and numerical characterization of paraffin-based fuels for hybrid rocket application*, 2019. doi:10.2514/6.2019-4195, URL `https://arc.aiaa.org/doi/abs/10.2514/6.2019-4195`.

[26] Leccese, G., Bianchi, D., Nasuti, F., Stober, K. J., Narsai, P., and Cantwell, B. J., "Experimental and numerical methods for radiative wall heat flux predictions in paraffin-based hybrid rocket engines," *Acta Astronautica*, Vol. 158, 2019, pp. 304–312. doi:10.1016/j.actaastro.2018.06.032.

[27] Fabiani, M., Gubernari, G., Migliorino, M., Bianchi, D., and Nasuti, F., "Numerical Simulations of Fuel Shape Change and Swirling Flows in Paraffin/Oxygen Hybrid Rocket Engines," *Aerotecnica Missili & Spazio*, 2022. doi:10.1007/s42496-022-00141-6.

[28] Karthikeyan, G., and Shimada, T., "Numerical Parametric Analysis of Combustion Instability in Axial-injected Hybrid Rocket Motors," *Journal of Propulsion and Power*, Vol. 34, No. 6, 2018, pp. 1542–1552. doi:10.2514/1.B36826.

[29] Ferrero, A., Masseni, F., and Pastrone, D., "Low-order models for low-frequency combustion instability in hybrid rocket engines," *AIP Conference Proceedings*, Vol. 2293, No. 1, 2020, p. 200003. doi:10.1063/5.0026694, URL `https://aip.scitation.org/doi/abs/10.1063/5.0026694`.

[30] Ferrero, A., Masseni, F., Muscarà, L., and Pastrone, D., "Multiphysics Modelling of a Hybrid Rocket Engine," *ECCOMAS Congress 2020 Proceedings*, 2021. doi:DOI:10.23967/wccm-eccomas.2020.213.

[31] Barato, F., Bellomo, N., Faenza, M., Lazzarin, M., Bettella, A., and Pavarin, D., "Numerical Model to Analyze Transient Behavior and Instabilities on Hybrid Rocket Motors," *Journal of Propulsion and Power*, Vol. 31, No. 2, 2015, pp. 643–653. doi:10.2514/1.B35282.

[32] Karabeyoglu, M. A., and Altman, D., "Dynamic Modeling of Hybrid Rocket Combustion," *Journal of Propulsion and Power*, Vol. 15, No. 4, 1999, pp. 562–571. doi:10.2514/2.5464.

[33] Brown, T. R., and Lydon, M. C., "Testing of Paraffin-Based Hybrid Rocket Fuel Using Hydrogen Peroxide Oxidizer," *AIAA Region 5 Student Conference, Wichita, USA*, 2005.

[34] Gordon, S., and McBride, B. J., "Computer Program for Calculation of Complex Chemical Equilibrium," *NASA reference publication*, Vol. 1311, 1994.

[35] Durand, J.-E., Lestrade, J.-Y., and Anthoine, J., "Fuel Regression Modelling for Hybrid Rocket CFD Simulations," *EUCASS 2019*, MADRID, Spain, 2019. doi:10.13009/EUCASS2019-634, URL `https://hal.archives-ouvertes.fr/hal-02420996`.

[36] Liou, M.-S., "A Sequel to Ausm: Ausm+," *Journal of computational Physics*, Vol. 129, No. 2, 1996, pp. 364–382. doi:10.1006/jcph.1996.0256.

[37] Barato, F., Bellomo, N., Lazzarin, M., Moretto, F., Bettella, A., and Pavarin, D., "Numerical modeling of paraffin-based fuels behavior," *48th AIAA/ASME/SAE/ASEE Joint Propulsion Conference & Exhibit*, 2012, p. 3750. doi:10.2514/6.2012-3750.

[38] Gottlieb, S., and Shu, C.-W., "Total Variation Diminishing Runge-Kutta Schemes," *Mathematics of computation*, Vol. 67, No. 221, 1998, pp. 73–85. doi:10.1090/S0025-5718-98-00913-2.

[39] Batina, J. T., "Unsteady Euler Airfoil Solutions Using Unstructured Dynamic Meshes," *AIAA journal*, Vol. 28, No. 8, 1990, pp. 1381–1388. doi:10.2514/3.25229.

[40] Altman, D., and Humble, R., *Space Propulsion Analysis and Design*, McGraw-Hill Companies,Incorporated, 1995, Chap. Hybrid Rocket Propulsion Systems, p. 372–383. doi:10.2514/6.2019-4195, URL `https://arc.aiaa.org/doi/abs/10.2514/6.2019-4195`.

[41] Carmicino, C., and Pastrone, D., "On the Explanation of the "DC Shift" in Hybrid Rockets," *2018 Joint Propulsion Conference*, 2018, p. 4525. doi:10.2514/6.2018-4525.

[42] Carmicino, C., and Pastrone, D., "Acoustic Excitation as Triggering Mechanism of the "DC Shift" in Hybrid Rockets," *AIAA Journal*, Vol. 57, No. 11, 2019, pp. 4845–4853. doi:10.2514/1.J058139, URL https://doi.org/10.2514/1.J058139.

[43] Karabeyoglu, M. A., De Zilwa, S., Cantwell, B., and Zilliac, G., "Modeling of Hybrid Rocket Low Frequency Instabilities," *Journal of Propulsion and Power*, Vol. 21, No. 6, 2005, pp. 1107–1116. doi:10.2514/1.7792.

[44] Marxman, G., Wooldridge, C., and Muzzy, R., "Fundamentals of Hybrid Boundary-layer Combustion," *Progress in Astronautics and Rocketry*, Vol. 15, Elsevier, 1964, pp. 485–522. doi:10.1016/B978-1-4832-2730-6.50025-7.

[45] Budzinski, K., Aphale, S. S., Ismael, E. K., Surina III, G., and DesJardin, P. E., "Radiation heat transfer in ablating boundary layer combustion theory used for hybrid rocket motor analysis," *Combustion and Flame*, Vol. 217, 2020, pp. 248–261. doi:https://doi.org/10.1016/j.combustflame.2020.04.011.

[46] Majdalani, J., Kuo, K., and Chiaverini, M., "Vortex injection hybrid rockets," *Progress in Astronautics and Aeronautics*, Vol. 218, 2007, pp. 247–276. doi:10.2514/5.9781600866876.0247.0276.

[47] Fleischmann, J., and Majdalani, J., "Complex lamellar helical solution for cyclonically driven hybrid rocket engines," *53rd AIAA Aerospace Sciences Meeting*, 2015. doi:https://doi.org/10.2514/6.2015-0372.

[48] Marquardt, T., and Majdalani, J., "Beltramian solution for cyclonically driven hybrid rocket engines," *53rd AIAA/SAE/ASEE Joint Propulsion Conference*, 2017. doi:https://doi.org/10.2514/6.2017-4638.

[49] Greatrix, D. R., "Geometric Swirl Number and Hybrid Rocket Engine Performance," *2018 Joint Propulsion Conference*, 2018, p. 4442. doi:10.2514/6.2018-4442.

[50] McBride, B. J., *Computer Program for Calculation of Complex Chemical Equilibrium Compositions and Applications*, Vol. 2, NASA Lewis Research Center, 1996.

[51] Goodwin, D. G., Moffat, H. K., Schoegl, I., Speth, R. L., and Weber, B. W., "Cantera: An Object-oriented Software Toolkit for Chemical Kinetics, Thermodynamics, and Transport Processes," https://www.cantera.org, 2022. doi: 10.5281/zenodo.6387882, version 2.6.0.

[52] Smith, W. R., and Missen, R. W., *Chemical reaction equilibrium analysis : theory and algorithms*, Wiley, 1982.

[53] Bellomo, N., Faenza, M., Barato, F., Bettella, A., Pavarin, D., and Selmo, A., "The" Vortex Reloaded" Project: Experimental Investigation on Fully Tangential Vortex Injection in N2O-paraffin Hybrid Motors," *48th AIAA/ASME/SAE/ASEE Joint Propulsion Conference & Exhibit*, 2012, p. 4304. doi:10.2514/6.2012-4304.